Mon. Not. R. Astron. Soc. **000**, 000–000 (0000) Printed 7 July 2011 (MN LATEX style file v2.2)

Precision cosmology with a wide area XMM cluster survey

M. Pierre[1⋆], F. Pacaud[2], J.B. Juin[3], J.B. Melin[4], P. Valageas[5], N. Clerc[1], P.S. Corasaniti[6]
[1]*DSM/Irfu/SAp, CEA/Saclay, F-91191 Gif-sur-Yvette Cedex, France*
[2]*Argelander Institut für Astronomie, Universität Bonn, Germany*
[3]*Departamento de Astronomía y Astrofísica, Pontificia Universidad Católica de Chile, Casilla 306, Santiago 22, Chile*
[4]*DSM/Irfu/SPP, CEA/Saclay, F-91191 Gif-sur-Yvette Cedex, France*
[5]*DSM/IPhT, CEA/Saclay, F-91191 Gif-sur-Yvette Cedex, France*
[6]*CNRS, Laboratoire Univers et Théories (LUTh), UMR 8102 CNRS, Observatoire de Paris, Université Paris Diderot, 5 Place Jules Janssen, 92190 Meudon, France*

arXiv:1009.3182v2 [astro-ph.CO] 6 Jul 2011

ABSTRACT

We explore the cosmological constraints expected from wide area XMM-type cluster surveys covering 50-200 deg^2, under realistic observing conditions. We perform a Fisher matrix analysis based on cluster number counts in combination with estimates of the 2-point cluster correlation function. The effect of the survey design is implemented through an observationally well tested cluster selection function. Special attention is given to the modeling of the shot noise and sample variance, which we estimate by applying our selection function to numerically simulated surveys. We then infer the constraints on the equation of state of the dark energy considering various survey configurations. We quantitatively investigate the respective impact of the cluster mass measurements, of the correlation function and of the $1 < z < 2$ cluster population. We show that, with some 20 Ms XMM observing time, it is possible to constrain the dark energy parameters at a level which is comparable to that expected from the next generation of cosmic probes. Such a survey has also the power to provide unique insights into the physics of high redshift clusters and AGN properties.

Key words: cosmology: observations - cosmology: theory - clusters: general - cosmological parameters

1 INTRODUCTION

The statistical properties of galaxy clusters provide independent cosmological information, complementary to that inferred from other observations such as measurements of the Cosmic Microwave Background (CMB), Supernova Type Ia (SN Ia), Baryon Acoustic Oscillations (BAO) and weak lensing (WL) data. Clusters are the largest virialized objects (dark matter halos) in the Universe, with mass scales corresponding to overdensities that enter the non-linear phase of gravitational collapse between redshifts $0 < z < 3$. Consequently, their abundance and spatial distribution can potentially probe both the cosmic expansion history as well as the growth of cosmic structures. Theoretical considerations such as the prediction of the halo mass function based on semi-analytical approaches (Press & Schechter 1974; Bond et al. 1991) and N-body simulations (see e.g. Sheth & Tormen 1999) have suggested that cluster statistics is particularly sensitive to the normalization of the matter power spectrum σ_8 (the root-mean-square of linear fluctuations within a sphere of $8h^{-1}$ Mpc radius) and the total cosmic matter density $\Omega_{\rm m}$. These observational aspects have given a strong incentive to the use of clusters as cosmic probes.

Over the past decades cluster observations have greatly evolved. After the pioneering studies of the Einstein Medium Sensitivity Survey (Gioia et al. 1990), the Rosat All-sky survey (RASS) and deep ROSAT pointed observations have provided an invaluable reservoir of clusters out to redshift ~ 1. These measurements enabled the first determinations of σ_8 and $\Omega_{\rm m}$ based on cluster number counts alone (see Evrard 1989; Oukbir & Blanchard 1992; White et al. 1993; Viana & Liddle 1996; Eke et al. 1998; Henry 1997, 2000; Borgani et al. 2001; Vikhlinin et al. 2003; Allen et al. 2003) and in combination with measurements of the local correlation function from RASS (Schuecker et al. 2003). Similarly the Sloan Digital Sky Survey cluster catalogue offered the first determination using an optical dataset (e.g. Bahcall et al. 2003). Quite remarkably these measurements have always consistently pointed out to a low matter density universe, in agreement with results from galaxy survey data (Percival et al. 2001; Tegmark et al. 2004) and CMB observations (De Bernardis et al. 2000; Spergel et al. 2003). With the launch of XMM and Chandra a decade ago, a new era has begun: deep pointed observations of large cluster samples, mainly extracted from the ROSAT catalogues, have provided detailed insights into the baryonic physics of clusters and their morphology. This has resulted in a tremendous burst in the modeling of the cluster properties as well as in the determination of their mass. These advancements have led to improved constraints on σ_8 and $\Omega_{\rm m}$, as obtained for example using the

⋆ E-mail:mpierre@cea.fr

temperature function of local bright clusters (Henry et al. 2009). From the point of view of large area surveys, the XMM-LSS survey (Pierre et al. 2004) covering some 11 deg^2 performed pioneering cluster detection work, assembling a complete sample of XMM clusters at a sensitivity of $\sim 10^{-14}$ erg cm^{-2} s^{-1} in the [0.5-2] keV band. Moreover, it provided detailed insights about the impact of selection effects on cluster evolutionary studies (Pacaud et al. 2007).

The discovery of dark energy has generated a revived interest in the use of cluster statistics as an alternative test for probing the nature of this exotic component. Dark energy can directly affect the cluster number counts by modifying the growth rate of structures as well as the size of the cosmological volume probed at a given redshift (Wang & Steinhardt 1998; Haiman, Mohr & Holder 2001; Huterer & Turner 2001). Several works have attempted to measure the dark energy equation of state using cluster data in combination with other probes (Henry 2004; Mantz 2008; Vikhlinin et al. 2009; Allen et al. 2008; Rozo et al. 2009). However statistical and systematic uncertainties, as well as the presence of degeneracy between cosmological parameters, remain the major limitations to accurately test dark energy with current data.

From an observational point of view, the main quantities that are useful to constrain cosmology are: the redshift evolution of the cluster number counts (dn/dz) or ideally the evolution of the cluster mass function ($dn/dMdz$), the spatial distribution of clusters (e.g. the two-point correlation function, ξ), the cluster temperature function, the gas mass fraction in clusters as well as various scaling laws describing the evolution of cluster structural properties. There are two key practical issues that such studies have to face: firstly the ability to assemble well characterized cluster samples, and secondly the need for well understood mass-observable relations, since for a given cosmology the cluster mass is the only independent variable entering the theory. Mass estimates can be inferred from a variety of methods: optical richness, galaxy velocity dispersion, X-ray luminosity or temperature, S-Z decrement, weak lensing signal or from more elaborated proxies such as $T_{\rm X} \times M_{\rm gas}$ described in (Kravtsov et al. 2006); if X-ray temperature and gas density profiles are available, masses can be calculated under the hypothesis of hydrostatic equilibrium.

Depending on the number of cosmological parameters that one aims at constraining and the required accuracy, the minimum size of useful cluster samples ranges from 50-100 objects for constraining σ_8 and $\Omega_{\rm m}$ only, to several hundreds or even several thousands (if little information is available on masses) for constraining the dark energy parameters.

Since clusters constrain regions of the cosmological parameter space which are complementary to that probed by other tests such as SN Ia, CMB, BAO and WL data (see e.g. Huterer & Turner 2001), considerable efforts have been devoted, both theoretically and observationally, to characterize the use of clusters in the near future. Forecasts of the dark energy parameter uncertainties from future optical, X-ray and S-Z surveys have been the subject of several analyses (Weller, Battye & Kneissl 2002; Hu & Kravtsov 2003; Majumdar & Mohr 2003, 2004; Wang et al. 2004; Wu, Rozo & Wechsler 2008). These studies, generally focusing on surveys covering a few 1 000 deg^2, have shown that precision cosmology in the context of cluster surveys is certainly possible in the near future. Subsequently, there has been a growing interest in evaluating the impact of systematic uncertainties of such cluster surveys. For instance, one can mention the sensitivity of the dark energy constraints to halo modeling uncertainties (Cunha & Evrard 2009) or to the mass accuracy of given cluster sub-samples; the latter is of special relevance when designing the follow-up observations to increase the cluster mass accuracy: given that telescope time is limited, it is necessary to optimise the targeting of specific mass and redshift ranges (Wu et al. 2010).

While these prospective dark energy studies pertain to upcoming or future instrumentation, we examine here the potential of XMM, whose characteristics and capabilities are now very well established. In fact, with its outstanding collecting area (~ 2000 cm^2 on axis at 1 keV), wide spectral range ([0.1-10] keV), good spatial (~ 6 arcsec on axis) and spectral (5-10% at 1 keV) resolution, XMM appears to be the best suited, currently available, X-ray observatory to undertake a large cluster survey. As an example, with 10 ks exposures, XMM reaches a sensitivity which is about 1000 times greater than RASS, i.e. 5×10^{-15}erg cm^{-2} s^{-1} in [0.5-2] keV for point sources. Basically, XMM has the power to unambiguously resolve any cluster[1] provided that at least some 100 photons are collected.

In this paper, we forecast the dark energy parameter errors for an XMM cluster survey with an area of the order of 100 deg^2. Using results from accurate survey simulations and precise model predictions, we estimate the dark energy parameter errors for different survey configurations. We find that the expected parameter constraints are not only complementary to those of other cosmological probes, but competitive with respect to forecasted errors for the next generation of dark energy dedicated experiments.

Compared with other cluster surveys, X-ray observations have an indisputable advantage, since cluster X-ray properties can be predicted *ab initio* for a given cosmological model, with *observational input* (e.g., mass-observable relations) being easily implementable. In contrast, ground-based large optical cluster surveys (e.g., SDSS Max BCG catalogue, Koester et al. 2007), though may appear much more attractive because of their lower cost, still require *ad hoc* prescriptions to evaluate the cluster selection function with cosmological numerical simulations. Such procedures usually rely on the optical richness as defined by the galaxy distribution. We want to stress that computing a cluster survey selection function in the era of precision cosmology requires a self-consistent modeling of the selection function itself. We will show here that this plays a critical role in the interpretation of the cluster number counts. It is also worth mentioning that, after 40 years of experience, X-ray cluster surveys are still much ahead of S-Z surveys both in terms of detection rates and for the evaluation of the selection function. In the following we shall refer to the discussed survey as the XXL survey.

The paper is organized as follows. In Section 2 we introduce the basic equations for the cluster survey observables, namely the cluster number counts and the 2-point correlation function. In Section 3 we describe the survey configurations and selection functions, while in Section 4 using numerical simulations we estimate the expected experimental survey uncertainties. In Section 5 we describe the Fisher matrix calculation performed to infer the expected cosmological parameter constraints, and discuss the results in Section 6. Finally we present our summary and conclusions in Section 7. Throughout the paper, we consider the ΛCDM cosmology with the parameters determined by WMAP-5 (Dunkley et al. 2009) as our fiducial cosmological model.

[1] A core radius of 150 kpc corresponds to an apparent diameter of 35 arcsec at $z = 2$, to be compared to the XMM on-axis PSF of 6 arcsec

2 CLUSTER SURVEY OBSERVABLES

The number of clusters as function of redshift is given by

$$\frac{dn}{dz} = \Delta\Omega \frac{d^2V}{d\Omega dz}(z) \int_0^\infty F_{\rm s}(M,z) \frac{dn(M,z)}{d\log M} d\log M, \quad (1)$$

where $\Delta\Omega$ is the survey solid angle, $d^2V/d\Omega dz$ is the cosmological volume factor, $F_{\rm s}(M,z)$ is the redshift dependent survey selection function and $dn/d\log M$ is the comoving density of halos of mass M.

The volume factor in a Friedmann-Robertson-Walker space-time reads as

$$\frac{d^2V}{d\Omega dz} = \frac{c}{H_0} \frac{(1+z)^2 d_{\rm a}^2(z)}{E(z)}, \quad (2)$$

with c the speed of light, H_0 the Hubble constant today, and

$$E(z) = \sqrt{\Omega_{\rm m}(1+z)^3 + \Omega_{\rm r}(1+z)^4 + \Omega_{\rm DE} I_{\rm DE}(z) + \Omega_k (1+z)^2}, \quad (3)$$

where $\Omega_{\rm m}, \Omega_{\rm r}, \Omega_{\rm DE}, \Omega_k$ are the present matter, radiation, dark energy, and curvature densities, in units of the critical density respectively, and $d_{\rm a}(z)$ is the angular diameter distance. The function $I_{\rm DE}(z)$ depends on the model of dark energy. We consider three scenarios: 1) cosmological constant Λ, with $I_\Lambda(z) = 1$; 2) dark energy fluid characterized by a constant equation of state w for which $I_{\rm DE}(z) = (1+z)^{3(1+w)}$; 3) time evolving dark energy equation of state parametrized in the form $w_{\rm DE}(z) = w_0 + w_a z/(1+z)$ (Chevallier & Polarski 2001; Linder 2003) for which $I_{\rm DE}(z) = (1+z)^{3(1+w_0+w_a)} \exp\left[-3w_a z/(1+z)\right]$.

Cluster DE studies make various assumptions as to the selection function. It can be defined by a simple mass limit, depending or not on redshift and cosmology; the limit is supposed to be step-like or to allow for a possible dispersion and for some smooth function across the threshold (e.g. Lima & Hu 2005; Hu & Cohn 2006; Albrecht et al. 2006; Basilakos et al. 2010). For an X-ray survey, $M_{\rm lim}(z)$ is determined using a mass-observable relation, for instance the mass-luminosity relation. Because of this, the limiting mass depends on empirically determined parameters (parametrizing the physics of the hot gas in clusters), and the luminosity distance, i.e. on the underlying cosmological model. This is an important point, since it implies that to properly infer cosmological constraints from cluster data one must take into account the cosmological dependence of the mass threshold $M_{\rm lim}(z)$. Another relevant aspect concerns the fact that survey design, instrumental characteristics and imaging technique analysis, cause the cluster selection function not to behave as a step function. This can affect the predicted number counts and 2-point correlation statistics for a given cosmological model. The effect of a non step-like function has been studied in the literature for S-Z surveys (Holder et al. 2000; Lin & Mohr 2003) and X-ray surveys (Sahlén et al. 2009). Here we use realistic selection functions derived from accurate simulations of the XMM-LSS survey that will be discussed in Section 3.

The comoving density of halos of mass M at redshift z reads as

$$\frac{dn(M,z)}{d\log M} = -\frac{\bar\rho_{\rm m}}{M} \frac{d\log\sigma}{d\log M} f(\sigma,z), \quad (4)$$

with $\bar\rho_{\rm m}$ the present mean matter density, $\sigma(M,z)$ the root-mean-square fluctuation of the linear density contrast smoothed on a scale $R = (3M/4\pi\bar\rho_{\rm m})^{1/3}$, and $f(\sigma,z)$ the multiplicity function. Here we adopt for $f(\sigma,z)$ the modeling proposed by Tinker et al. (2008). Our working assumptions are detailed in Appendix A.

The variance of the linear density contrast smoothed on scale R at redshift z is given by

$$\sigma^2(R,z) = A^2 \int \frac{dk}{2\pi^2} k^{n_s+2} T^2(k,z) W^2(kR), \quad (5)$$

where A is a normalization constant fixed so that today $\sigma(R = 8h^{-1}{\rm Mpc}) = \sigma_8$, n_s is the scalar spectral index, $T(k,z)$ is the linear matter transfer function and $W(kR)$ is the Fourier transform of the real space top-hat window function. We compute the matter transfer function using the fitting formula provided by Eisenstein & Hu (1998), which includes the wave pattern imprinted by the baryon acoustic oscillations.

On large scales the 2-point spatial correlation function for a cluster survey covering the redshift range $[z_{\rm min}, z_{\rm max}]$ is given by

$$\xi(R) = \frac{\int_{z_{\rm min}}^{z_{\rm max}} \frac{d^2V}{d\Omega dz} n^2(z) \xi(R,z) dz}{\int_{z_{\rm min}}^{z_{\rm max}} \frac{d^2V}{d\Omega dz} n^2(z) dz}, \quad (6)$$

where

$$n(z) = \int_0^\infty F_{\rm s}(M,z) \frac{dn(M,z)}{d\log M} d\log M, \quad (7)$$

and $\xi(R,z) = b_{\rm eff}^2(z) \xi_{\rm lin}(R,z)$, with $\xi_{\rm lin}(R,z)$ the Fourier transform of the linear matter power spectrum at redshift z. The evolution of the linear bias averaged over all halos reads as (Matarrese et al. 1997)

$$b_{\rm eff}(z) = \frac{1}{n(z)} \int_0^\infty F_{\rm s}(M,z) b(M,z) \frac{dn(M,z)}{d\log M} d\log M, \quad (8)$$

where $b(M,z)$ is the linear bias relating dark matter halos of mass M to the mass density fluctuation. We assume the bias model introduced in Tinker et al. (2010),

$$b(M,z) = 1 - \frac{1+A_b}{1+\sigma^{a_b}} + 0.183 \left(\frac{\delta_c}{\sigma}\right)^{1.5} + B_b \left(\frac{\delta_c}{\sigma}\right)^{2.4}, \quad (9)$$

with $\delta_c = 1.686$ the critical linear overdensity given by the spherical collapse model, and the fitting parameters given by

$$A_b = 0.24 y \exp\left[-(4/y)^4\right], \quad (10)$$

$$a_b = 0.44(y-2), \quad (11)$$

$$B_b = 0.019 + 0.107 y + 0.19 \exp\left[-(4/y)^4\right], \quad (12)$$

where $y = \log_{10}(\Delta_{\rm m})$ with $\Delta_{\rm m}$ the nonlinear overdensity threshold. Our fixed value of δ_c is only exact for an Einstein-de Sitter universe - although it hardly varies with the cosmology. Nevertheless, we preferred to follow the convention of Tinker et al. (2010) and fix it.

3 XXL SURVEY CHARACTERISTICS

Cluster surveys are, similarly to galaxy surveys, defined by a number of parameters such as sky coverage and geometry, depth, selection function, and redshift accuracy. On the other hand, compared to galaxies, clusters are rare objects, a characteristic that has a significant impact on the determination of the correlation function. Moreover, as already mentioned in the introduction, cluster mass accuracy plays an important role in the determination of the cosmological parameters. In this section, we present the generic characteristics of the XXL survey, while a quantitative examination of the various sources of uncertainty will be presented in Section 4.

3.1 Two survey designs

In this case study, we examine the merits of two possible XMM survey concepts: *Survey-A* covers a total sky area of 50 deg^2 with 40 ks XMM pointings, this configuration is assumed to allow mass measurements at the 10-50% level for the selected cluster samples; *Survey-B* covers 200 deg^2 with 10 ks XMM pointings and provides a cluster mass accuracy of 50-80%. Possible survey configurations, resulting from various splitting in sub-regions, are summarized in Table B1 and discussed in Section 4.2.

To give an order of magnitude of the observing time necessary to perform these surveys, one can imagine mosaics consisting of XMM observations whose center are separated by 20 arcmin in RA and Dec, so that 9 observations are necessary to cover 1deg^2. Consequently, both surveys A and B correspond approximately to $\sim$ 18 Ms net observing time, i.e. some 180 XMM (2-day) revolutions, allowing for 10 observations per revolution with the mosaic mode.

3.2 Modeling the cluster population as seen by XMM

Before detailing the survey selection function, we need to specify how the two basic observable quantities, the X-ray count rate in a given band and the apparent size of the cluster sources, relate to the cluster mass as a function of redshift.

In the following, we assume the usual [0.5-2] keV range as the working detection band, since it presents the optimal S/N, given the cluster spectra, the background spectrum and the XMM spectral response (Scharf 2002). Furthermore we assume the observed cluster scaling laws between luminosity (L), temperature (T) and the mass within a radius containing an overdensity of 200 times the critical density (M_{200c}) as determined in the local universe (Arnaud & Evrard 1999; Arnaud et al. 2005), and use the self-similar prescription for their evolution. To account for the scatter observed in cluster properties, we encapsulate the dispersion of the $M-T$ and $L-T$ relations in the $M-L$ relation, for simplicity. Following the analysis by Stanek et al. (2006), who measured $\sigma_{\ln M|L} = 0.37$, we use $\sigma_{\ln L|M} \sim 0.37 \times 1.59 \sim 0.6$, where 1.59 is the slope of their $M-L$ relation. To assign the X-ray luminosity we assume a log-normal distribution. These prescriptions allow us to compute the flux, and finally the count rate as function of the cluster mass and redshift. The impact of these hypotheses will be discussed in Sec. 6 and 7.

Fluxes are estimated using the APEC thermal plasma model, assuming a fixed hydrogen column density of 2.6×10^{20} cm^{-2} and setting the heavy element abundance to 0.3 solar. Fluxes are subsequently folded with the telescope and detector response (EPIC response matrices) assuming the THIN optical blocking filter. This allows us to predict the observed count-rates. We further assume a β-profile for the gas distribution, with β=2/3 and a constant physical core radius of 180 kpc, unless otherwise specified. This finally yields the spatial distribution of the cluster counts on the detectors.

3.3 The cluster selection function

We now turn to the description of the selection function. The ability to select clusters upon well-defined X-ray criteria is a key issue: as shown in Section 2, the selection function directly enters into the modeling of the cluster number counts and spatial correlation function.

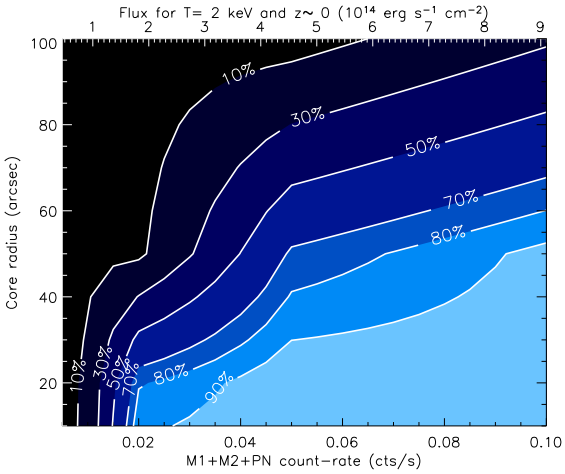


Figure 1. The C1 cluster selection function derived from extensive simulations: the probability of cluster detection is expressed in the count rate ($\sim$ flux) - core radius plane. A β-model with $\beta = 2/3$ is assumed.

In this prospective study, we adopt the C1/C2 selection functions specifically determined for the XMM-LSS survey. These have been extensively tested on the basis of XMM image simulations (Pacaud et al. 2006) and applied to the XMM-LSS sample (Pacaud et al. 2007). The selection basically operates in the *[extent, extent likelihood]* X-ray pipeline parameter space[2], where *extent* is taken to be the core radius of the β-model. The procedure allows us to assemble samples of extended X-ray sources that have a well-defined degree of contamination by miss-classified point-source; these can be easily discarded a posteriori by examining the X-ray/optical overlays. We define two samples, C1 and C2, for which the contamination is $\sim$ 0 and $\sim$ 50% respectively (Pierre et al. 2006). This procedure, which operates in a two-dimensional parameter space, enables the construction of uncontaminated cluster samples significantly larger than those obtained by a simple flux limit. The selection criteria are subsequently converted into the probability of detecting a source characterized by a given core radius and flux. The C1 selection probability function is displayed in Fig. 1. Using the cluster model described in the previous paragraph, we derive the limiting cluster mass detectable as a function of redshift for C1 and C2 respectively. Since the current C1/C2 selection criteria have been defined for 10 ks XMM exposures, the resulting selection corresponds to clusters having $M_{200c} > 2 \times 10^{14}\ M_{\odot}$, thus relatively massive objects as can be seen in Fig. 2. Moreover we note that $M_{\rm lim}(C1) \sim 1.5 \times M_{\rm lim}(C2)$ for $z > 0.2$, with the C2 selection yielding about twice as many clusters as the C1 selection. Notice that the C1 sample is always a sub-sample of the C2 selection. The number of collected cluster counts at the detection limit is displayed in Fig. 3.

Practically, our cosmological analysis will be performed in two stages. (i) In a first step, we consider the same cluster selection functions independently of the survey configuration (A or B). This means that for configuration A, the sample is defined from

[2] Because of the limited number of source photons, the pipeline operates in Cash statistics and returns, for each source parameter, the likelihood of the measurement

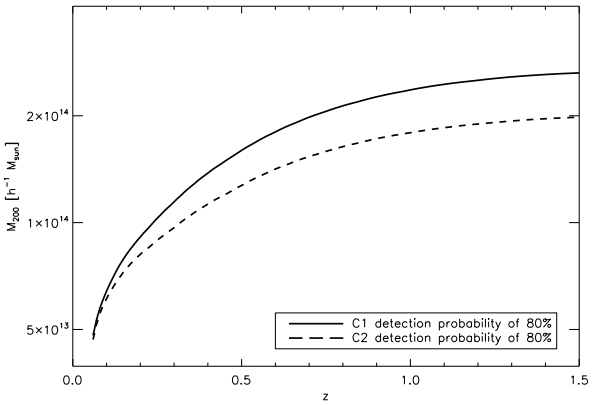


Figure 2. The limiting detectable cluster mass as a function of redshift. A detection probability of 80% is assumed. Masses are expressed in terms of M_{200c}, the mass within a radius containing an overdensity 200 times the *critical density*.

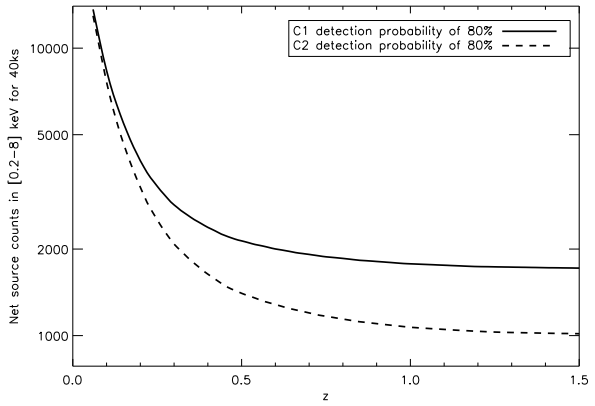


Figure 3. Number counts (2 MOS + pn) collected in 40 ks (*Survey-A* configuration) from a C1 and C2 cluster in the [0.2-8] keV energy range, as a function redshift. A detection probability of 80% is assumed, thus corresponding to the $M_{\rm lim}(z)$ of Fig. 2. The EPIC sensitivity has been averaged over the inner $r = 10$ arcmin (mean vignetting of 0.69). Assuming that half of the collected photons are used for the spectral analysis, our selection ensures that at least 500 counts are available for temperature determination with 40 ks XMM exposures.

sub-exposures of 10 ks. The main goal of the total 40 ks integration time is to reach the X-ray spectral accuracy enabling accurate mass measurements. Further, at the full depth of 40 ks, *Survey-A* enables the detection of deeper cluster samples. Consequently (ii) in a second step, we investigate the added cosmological value from clusters only detected in the 40 ks observations of *Survey-A*. We thus define a C20 class, a scaled-down version of the C2 population detected in 10 ks. Since the C2 selection function is well depicted by a detection probability as a function of S/N, we simply derived the C20 detection efficiency by extrapolating the results of Pacaud et al. (2006) to 40ks, scaling up the source S/N[3]. The density inferred for this population is on the order of 30/deg^2and comparable to that inventoried in the $\sim$ 50ks COSMOS field by

[3] This method was already applied in Pacaud et al. (2007) to account for the spatial variations of exposure time.

Table 1. Properties of the cluster samples selected for the cosmological analysis

Selection	Detected in configuration	Number density (deg^{-2})	
		$z < 1$	$z < 2$
C1	A B	7.1	8.0
C2	A B	11.6	13.7
C20	A	23.2	28.2

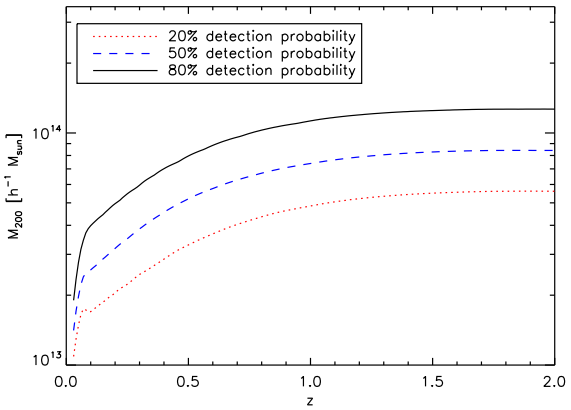


Figure 4. Same as Fig. 2 for the C20 population

Finoguenov et al. (2007). The characteristics of the C20 clusters are displayed in Figs. 4 and 5. The number densities of the C1, C2, C20 populations are given in Table 1. Furthermore, we define the following sub-classes: we refer to C2' for C2 clusters not detected as C1 and, similarly, to C20' for the C20 clusters not detected as C2.

4 ESTIMATING MEASUREMENT UNCERTAINTIES

We provide in this section a detailed account of the uncertainties pertaining to the measurements of clusters masses, cluster number counts and 2-point correlation function, as expected from the XXL

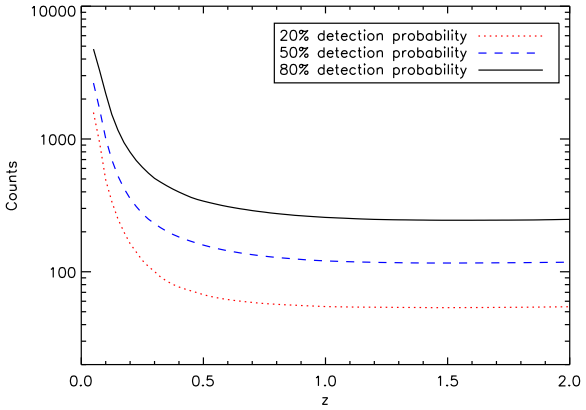


Figure 5. Same as Fig. 3 for the C20 population

Table 2. Adopted mass precision for each individual cluster as a function of XMM exposure time. The numbers are the 1-σ errors on $\ln(M)$. The * indicates that this sub-population does not provide mass information for the Fisher analysis. Last line gives the assumed precision on the luminosity measurements.

Selection	Adopted mass accuracy			
	Optimistic view		Pessimistic view	
	10 ks	40 ks	10 ks	40 ks
C1	0.5	0.1	0.8	0.5
C2'	0.8	0.5	*	0.8
C20'	not detected	0.8	not detected	*
$\sigma_{\ln L_{obs}}$	negligible		0.2	

survey. These are the necessary ingredients for a realistic evaluation of the cosmological parameter errors via a Fisher matrix analysis.

4.1 Accuracy of the cluster mass and redshift measurements

For this study, we do not rely on the, so far non-observationally validated, self-calibration techniques that allow for some universal redshift-dependent mass-observable relation (Majumdar & Mohr 2004); we discuss the relevance of this option in Sec. 7. We rather attribute to each cluster a mass accuracy as a function of its X-ray flux. The limiting collected counts for the three cluster populations, as indicated by Figs. 3 and 5, allow us to estimate the mass accuracy reachable for each selection. We consider a pessimistic and an optimistic situation and further set a limit on the precision of the observed luminosities. These working hypotheses are listed in Table 2. It is not the purpose of the present article to discuss in detail how such mass accuracy will be obtained, but one can foresee a set of realistic observations leading to the desired precision. For instance, configuration B is similar to the well studied XMM-LSS design, i.e. a mosaic of 10 ks exposures, which allowed mass measurements to better than 50% for the C1 population, under the assumption of hydrostatic equilibrium (Pacaud et al. 2007). Improved cluster mass accuracy will be attained with the addition of weak lensing and Sunyaev-Zel'dovich observations (e.g. Mahdavi et al. (2007)). The use of several X-ray mass proxies, such as the $Y_{\rm X} = T \times M_{\rm gas}$ parameter, can also greatly enhance the precision of the mass estimates (Vikhlinin et al. 2009).

Experience with the Canada France Hawaii Telescope Legacy Survey (CFHTLS[4]) showed that cluster photometric redshifts can be obtained for the C1 and most of the C2 clusters at an accuracy of $\sim 0.01-0.02$ from a 5-band survey in the optical (Mazure et al. 2007). Further, with the up-coming generation of wide-field spectroscopy instruments (e.g. refurbished VIMOS and forthcoming KMOS at the ESO Very Large Telescope) gathering redshifts of clusters with a density of $\sim 10-50/\deg^2$ over an area of 100 $\deg^2$ will be easily achievable within the next decade.

4.2 Statistical significance of dn/dz and ξ

Evaluating the impact of the survey size on the statistical significance of dn/dz and ξ from cluster surveys deserve special attention. Because clusters are rare objects, the relative effects of shot noise, sample variance and edge effects as functions of the survey depth and geometry are quite different from that of galaxy or weak lensing surveys. More precisely, considering splitting the survey in several sub-regions (a strategy favored by practical observing considerations), we need to estimate the trade-off between averaging the sample variance and the loss of S/N in the 2-pt correlation function at large distances. In principle, it is possible to analytically calculate the sample variance and the shot noise for dn/dz and ξ as a function of cosmology for a given flux limited or volume limited survey (e.g. Hu & Kravtsov 2003). Having here a well defined selection function $M_{\rm lim}(z)$, we perform an "in situ" and global estimate using numerically simulated cluster samples. The corresponding calculations are detailed in Appendix B

5 FISHER MATRIX ANALYSIS

We perform a Fisher matrix analysis to quantitatively estimate the cosmological information that can be extracted from the two XMM-survey configurations (A and B).

5.1 Method

Here we briefly sketch the basic principle of the Fisher matrix approach, interested readers may find more exhaustive discussions on its cosmological applications in (Tegmark, Taylor & Heavens 1997; Eisenstein, Hu & Tegmark 1999).

Let us consider a set of measurements $D_i = \{D_1, ..., D_N\}$ (for simplicity let us assume them to be uncorrelated), from which we want to derive constraints on a set of parameters $\theta_\mu = \{\theta_1, ..., \theta_M\}$ in a given model $\mathcal{M}$. We firstly evaluate the likelihood function, $L(D_i|\theta_\mu, \mathcal{M})$, and assuming a prior probability distribution for the model parameters, $P(\theta_\mu|\mathcal{M})$, we construct using Bayes' theorem the posterior probability, i.e. the probability of the parameters given the observed data, $P(\theta_\mu|D_i, \mathcal{M}) \propto L(D_i|\theta_\mu, \mathcal{M})P(\theta_\mu|\mathcal{M})$. The posterior contains all statistical information from which we derive the "confidence" intervals on the parameters θ_μ. Now, let us indicate with $\mathrm{O}_i(\theta_\mu)$ the model prediction of the observable to be confronted with the data D_i, and let σ_i be the experimental uncertainties. Assuming Gaussian distributed errors, we can write up to an additive constant the log-likelihood as

$$\ln L = -\frac{\chi^2}{2} = -\frac{1}{2}\sum_{i=1}^{N}\frac{[D_i - \mathrm{O}_i(\theta_\mu)]^2}{\sigma_i^2}. \qquad (13)$$

If $\hat{\theta}_\mu$ are the model parameter values that maximize the likelihood, then we can expand Eq. (13) to second order in $\delta\theta_\mu = \theta_\mu - \hat{\theta}_\mu$ and obtain

$$\mathcal{L} \equiv -\ln\left(\frac{L}{L_{\max}}\right) = \frac{1}{4}\sum_{\mu,\nu=1}^{M}\left.\frac{\partial^2\chi^2}{\partial\theta_\mu\partial\theta_\nu}\right|_{\hat{\theta}}\delta\theta_\mu\delta\theta_\nu. \qquad (14)$$

This leads to the Fisher matrix $F_{\mu\nu}$ given by[5]

$$F_{\mu\nu} \equiv \langle\frac{\partial^2\mathcal{L}}{\partial\theta_\mu\partial\theta_\nu}\rangle = \sum_{i=1}^{N}\frac{1}{\sigma_i^2}\frac{\partial \mathrm{O}_i}{\partial\theta_\mu}\frac{\partial \mathrm{O}_i}{\partial\theta_\nu}\Big|_{\hat{\theta}}. \qquad (15)$$

The parameter uncertainties as well as their mutual correlations are encoded in the covariance matrix, $C_{\mu\nu} = F^{-1}_{\mu\nu}$, where the 1σ

[4] http://www.cfht.hawaii.edu/Science/CFHLS/

[5] Although we have assumed a Gaussian likelihood to derive this expression, it is worth noting that the Fisher matrix has exactly the same shape for Poisson statistics.

model parameter errors are simply the square-root of the diagonal elements, $\sigma_{\theta_\mu} = \sqrt{C_{\mu\mu}}$. These are the marginalized errors, in the sense that if we consider a specific parameter, e.g. θ_1, then the uncertainty σ_{θ_1} obtained by inverting the full Fisher matrix is equivalent to that obtained by integrating the likelihood function over the $M-1$ parameters, thus accounting for all possible parameter correlations. External priors on a given parameter can be easily implemented, e.g. suppose we want to include a $\sigma_{\theta_3} = 0.01$ prior on the parameter θ_3, in such a case it is sufficient to add to Eq. (15) a matrix $P_{\mu\nu}$ whose only non-vanishing element is $P_{33} = 1/\sigma^2_{\theta_3}$. Similarly information from other datasets can be easily implemented by adding the corresponding Fisher matrices.

Using Eq. (15) greatly simplifies the estimation of the cosmological parameter uncertainties for a given experiment. Then forecasting parameter errors reduces to knowing the expected experimental/observational uncertainties (σ_i), assuming a fiducial cosmology ($\hat{\theta}_\mu$) and computing the Fisher matrix by evaluating the derivative of the observable at the fiducial parameter values ($\partial \mathrm{O}/\partial\theta_\mu|_{\hat{\theta}_\mu}$). The inferred errors will necessarily depend on the fiducial cosmology assumed; this is the case even if one runs a full numerical likelihood analysis over a set of randomly generated data. Henceforth the results of this type of analysis should not be used for estimating the performance of experiments in distinguishing between different models. We refer the reader to (Mukherjee et al. 2006) for a discussion on the limitation of this approach in model selection problems and the solution in the context of Bayesian statistics.

We evaluate the derivatives of the observable with the respect to the model parameters using the five-point stencil approximation:

$$\frac{\partial \mathrm{O}}{\partial\theta_\mu} \approx \frac{2}{3}\frac{O(\hat{\theta}_\mu+\delta\theta_\mu)-O(\hat{\theta}_\mu-\delta\theta_\mu)}{\delta\theta_\mu} + \frac{\mathrm{O}(\hat{\theta}_\mu-2\delta\theta_\mu)-O(\hat{\theta}_\mu+2\delta\theta_\mu)}{12\delta\theta_\mu} \quad (16)$$

with steps $\delta\theta_\mu$ of order 5% on the fiducial parameter value.

Our survey observables consist of the cluster number counts dn/dz given by Eq. (1) in redshift bins of size $\Delta z = 0.1$ and the two-point spatial correlation function $\xi(R)$ given by Eq. (6). For the cluster counts we consider detections in 10 or 20 equally spaced redshift bins in the range $0 < z < 1$ or $0 < z < 2$, while for the correlation function we consider the $10 < R\ (h^{-1}\mathrm{Mpc}) < 40$ scales. For each selection function we derive the expected survey uncertainties σ_i on dn/dz and ξ using the S/N calculated from the simulations, described in Appendix B. These account for the integrated effect of the Poisson noise and sample variance.

5.2 Fiducial cosmology and model parameters

We assume as our fiducial cosmology a flat ΛCDM model best-fitting the WMAP-5 years data (Dunkley et al. 2009), specified by the following parameter values: $\Omega_\mathrm{m}h^2 = 0.1326$, $\Omega_\mathrm{b}h^2 = 0.0227$, $h = 0.719$, $n_s = 0.963$, $\sigma_8 = 0.796$, $\tau = 0.087$. For this model the expected number of clusters as function of redshift for *Survey-A* ($50\mathrm{deg}^2$) is shown in Fig. 6 for the three selection functions. Fig. 7 displays the 2-point cluster correlation function. Here it is worth noticing that while the three functions have the same shape, the C2 curve has a slightly lower amplitude than C1, and higher than C20, consistently with the mass ranges pertaining to these samples (less massive objects are less clustered).

We derive constraints on the following set of parameters: $\Omega_\mathrm{m}, \Omega_\mathrm{b}, h, n_s, \sigma_8$ (ΛCDM), including a varying equation of state $w(z) = w_0 + w_a z/(1+z)$ with parameters w_0 and w_a (Chevallier & Polarski 2001; Linder 2003) for $w(z)$CDM models.

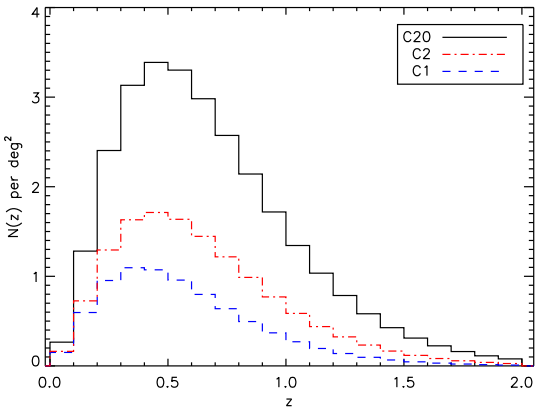


Figure 6. Redshift distribution of the C1, C2 and C20 populations for the ΛCDM fiducial cosmology in the *Survey-A* configuration.

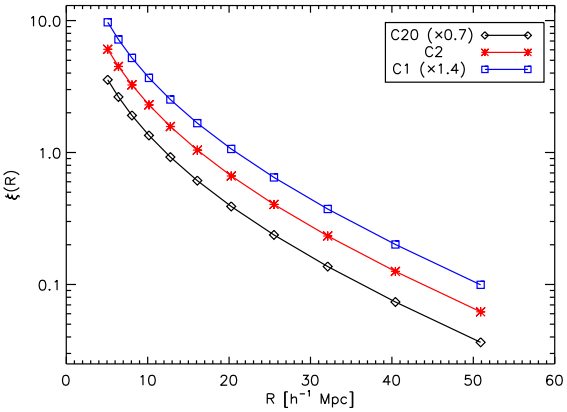


Figure 7. Two-point correlation function of the C1, C2 and C20 populations.

5.3 Modeling cluster mass uncertainties in the Fisher analysis

For the Fisher analysis, our aim is to reproduce as much as possible the observational procedure and the subsequent cosmological analysis. To summarize the steps: (1) clusters are selected in the XMM images according to a two-dimensional parameter space; (2) corresponding dn/dz and ξ are derived; (3) each cluster mass is measured at a given accuracy - the mass measurements being cosmology-dependent; (4) for a given cosmology, we compute dn/dz and ξ, the observational selection function being yet translated in the [M,z] space following scaling laws - this is the point where the mass accuracy enters; (5) as already specified, we encapsulate all uncertainties on the scaling laws in the M-L relation for the cosmological modeling; (6) the set of cosmological parameters giving best agreement both on dn/dz and ξ, describes the most likely cosmological model.

Practically, in the Fisher analysis, we assume that the slope and the dispersion of the M-L relation are known and do not depend on redshift. We let, however, the normalization of the relation free

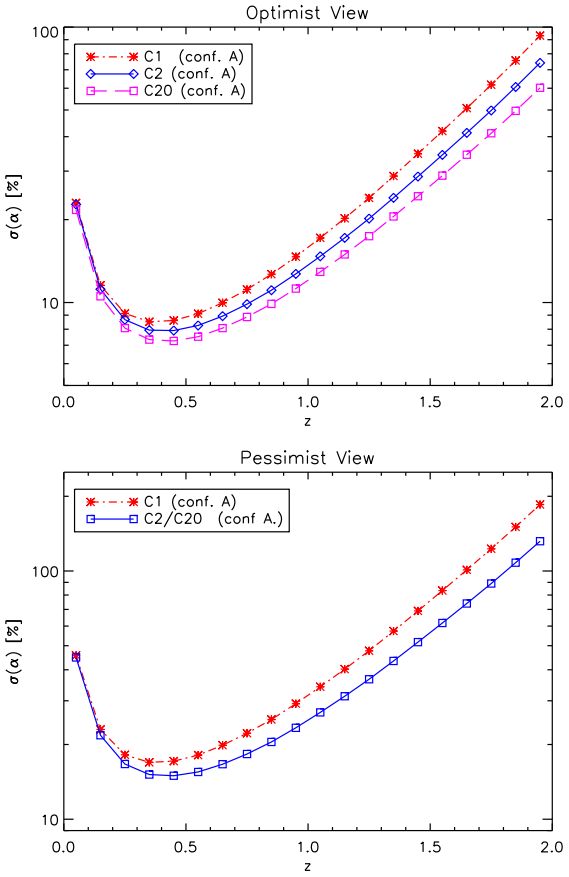


Figure 8. Priors for the Fisher analysis on the normalization of the M-L relation as a function of redshift, for the optimistic and pessimistic cases for the *Survey-A* configuration

as a scale factor $\alpha(z)$. We take one scale factor for each redshift bin ($\Delta(z) = 0.1$), hence we have 10 or 20 nuisance parameters depending on the survey depth. The priors for the analysis are derived from the accuracy assumed for the mass measurements of the individual clusters (Table 2); they are displayed in Fig. 8 for the optimistic and pessimistic cases.

5.4 Planck Fisher Matrix

To estimate the full cosmological yield of an XXL-survey, we perform a joint analysis of the cluster survey with the primary CMB power spectra (temperature-TT, polarization-EE and cross-correlation TE) soon to be measured by the Planck satellite.

A precise assessment of the Planck capabilities would require to model in detail the map making and component separation processes. To circumvent this problem, we make the simplifying assumption that the sky images in the three bands where the CMB emission dominates (100, 143 and 217 GHz) are readily usable to measure the power spectra, while the other bands permit a perfect characterization of the other contaminating signals.

Table 3. Planck survey parameters.

	Planck		
Frequency (GHz)	100	143	217
ϕ_c (arcmin)	10.0	7.1	5.0
$\sigma_{c,T}$ (μK)	6.8	6.0	13.1
$\sigma_{c,E}$ (μK)	10.9	11.4	26.7

Following (Zaldarriaga & Seljak 2007), the noise covariance matrix for each l (including the cosmic variance) is then given by:

$$\begin{aligned}
\mathrm{Cov}(C_l^{TT}, C_l^{TT}) &= \frac{2}{(2l+1)f_{\rm sky}}(C_l^{TT} + N_{l,TT}^{-2}),\\
\mathrm{Cov}(C_l^{EE}, C_l^{EE}) &= \frac{2}{(2l+1)f_{\rm sky}}(C_l^{EE} + N_{l,EE}^{-2}),\\
\mathrm{Cov}(C_l^{TE}, C_l^{TE}) &= \frac{1}{(2l+1)f_{\rm sky}}[C_{l,TE}^2\\
&+ (C_l^{TT} + N_{l,TT}^{-2})(C_l^{EE} + N_{l,EE}^{-2})],\\
\mathrm{Cov}(C_l^{EE}, C_l^{TE}) &= \frac{2}{(2l+1)f_{\rm sky}}C_l^{TE}(C_l^{EE} + N_{l,EE}^{-2})\\
\mathrm{Cov}(C_l^{TT}, C_l^{TE}) &= \frac{2}{(2l+1)f_{\rm sky}}C_l^{TE}(C_l^{TT} + N_{l,TT}^{-2})\\
\mathrm{Cov}(C_l^{TT}, C_l^{EE}) &= \frac{2}{(2l+1)f_{\rm sky}}C_{l,TE}^2,
\end{aligned} \tag{17}$$

where

$$N_{l,X}^2 = \sum_c (\sigma_{c,X}\phi_c)^{-2} e^{-l(l+1)\phi_c^2/(8\log 2)}, \tag{18}$$

is the contribution of the instrumental noise to the uncertainty on the spectrum X, which results from averaging over the different frequency channels c, with sensitivity $\sigma_{c,X}$ and angular bean-width ϕ_c. In Table 3, we quote the assumed experimental characteristics for the Planck satellite, which we obtained from the mission definition document (the so-called '*Bluebook*')[6]. We adopt a fractional sky coverage of $f_{\rm sky} = 0.8$ to account for the masking of the galactic plane.

The full CMB Fisher matrix for a set of cosmological parameters (θ_μ) is straightforwardly obtained as:

$$F_{\mu\nu}^{\rm CMB} = \sum_l \sum_{X,Y} \frac{\partial C_l^X}{\partial\theta_\mu} \mathrm{Cov}^{-1}(C_l^X, C_l^Y) \frac{\partial C_l^Y}{\partial\theta_\nu}, \tag{19}$$

where $X, Y = TT, EE, TE$ and we sum over l values in the range [1,2000].

In practice, we compute the power spectra using the CMB-FAST code and some care has to be taken in order to correctly account for the intrinsic CMB degeneracies. Indeed, the shape of the matter power spectrum at the recombination epoch is only a function of the primordial power spectrum and the physical densities ($\rho_{\rm m}$, $\rho_{\rm b}$, $\rho_{\rm r}$) in the early universe. Further, while the relative amplitudes of the CMB peaks depend on the details of the matter/photon

[6] available from the ESA web pages of the Planck mission: http://www.rssd.esa.int/index.php?project=Planck

Table 4. Fisher matrix errors on the cosmological parameters from Planck.

	10% prior on h		Flat universe	
	TT	TT+TE+EE	TT	TT+TE+EE
h	0.0719	0.0719	0.0030	0.0017
$\Omega_{\rm b}$	0.0088	0.0088	0.0007	0.0005
$\Omega_{\rm m}$	0.0514	0.0513	0.0019	0.0010
Ω_Λ	0.0880	0.0879	-	-
σ_8	0.0536	0.0361	0.0400	0.0067
n_s	0.0070	0.0040	0.0070	0.0040
τ	0.0532	0.0040	0.0532	0.0040

densities, the physical scale of the baryon oscillation pattern is simply proportional to the sound horizon at recombination ($r_{\rm s}$). As a consequence, the CMB observables only depend on h, $\Omega_{\rm DE}$, w_0 and w_a through the so-called CMB acoustic scale:

$$l_{\rm a} = \pi(1+z_{\rm dec})\frac{d_{\rm a}(z_{\rm dec})}{r_{\rm s}} \qquad (20)$$

where $z_{\rm dec}$ is the redshift of decoupling and $d_{\rm a}$ the angular diameter distance. [the factor $(1+z_{\rm dec})$ comes from the fact that $r_{\rm s}$ is measured in the comoving frame]. This exact degeneracy of the CMB, known as the geometric degeneracy, prevents CMB experiments from giving any constraint on the dark energy without adding other observables. Numerical estimates of CMB Fisher matrices, based on codes such as CMBFAST, fail at accurately reproducing this degeneracy (see e.g. Kosowsky et al. (2002)) and tend to give unrealistic results solely because of numerical uncertainties. We therefore follow the approach of the DETF report and Rassat et al. (2009) to estimate the Fisher matrix over a 'natural' set of cosmological parameters ($\Omega_{\rm m}h^2$, $\Omega_{\rm b}h^2$, $l_{\rm a}$, $\Delta^2_{\mathcal{R}}$, n_s and τ). We then marginalize over τ and convert the Fisher matrix into our preferred parameter set using the Jacobian matrix of the transformation.
In Table 4 we quote the resulting constraints for Planck alone with or without the use of polarization. Because of the geometrical degeneracy, only constraints on the simplest ΛCMD models can be obtained, however we have also estimated the full Fisher Matrix for the w(z)CDM model, since it is necessary to derive the combined constraints from the Planck CMB spectra with the cluster observables. This is then simply achieved by adding Eq. (19) to Eq. (15).

6 PREDICTED CONSTRAINTS ON THE COSMOLOGICAL PARAMETERS

Results from the Fisher analysis for the equation of state of the dark energy are presented in Tables 5 and 6 for the A2 and B0 survey configurations. We display the ultimate accuracy that can be reached for the most general, non flat, w(z)CDM cosmology. We outline below the main outcome of the study.
(1) The comparison between the C1 and C2 populations (limited to $0<z<1$) shows an improvement on w_0, w_a of about 20, 10% for the C2 sample. The C2 clusters are roughly twice as numerous as the C1, but less massive in average so that their impact on cosmological measurements is expected to be indeed relatively smaller.
(2) Focussing on the *Survey-A* configuration, the C20 clusters are four times more numerous than the C1 and some 250 of them are between $1<z<2$. The net effect is an improvement better than a factor of two on w_a and w_0.
(3) The comparison between the B and A survey designs for the C2 and C20 populations respectively shows comparable constraints when $dn/dz,\ \xi$ and Planck are combined (optimistic and pessimistic cases). However, the total number of clusters involved is 2320 for B compared to only 1400 for A. This stresses the efficiency of the $1<z<2$ clusters for characterising the dark energy (see also Baldi & Pettorino (2010)).
(4) Table 7 lists the constraints expected after the first scan of survey A, thus at 1/4 of its nominal depth (C2 population only and measured in pessimistic conditions): the accuracy is about half of that at full depth, hence along the line of the $\rm signal \propto \sqrt{time}$ ratio.
We have further investigated the role of various hypotheses that were made in the prescription of the Fisher analysis.
(5) This study is amongst the first ones to qualitatively consider the added value of the cluster spatial distribution in the determination of the DE parameters (see also Majumdar & Mohr 2004; Hütsi 2010). The impact of ξ is highlighted in Fig. 9. It is remarkable given that the regions considered for *Survey-A2* are only 3.5 deg aside, but should not be considered as unexpected. In fact, ξ is particularly sensitive to $\Omega_{\rm m}$ and σ_8, thus it strongly contributes to breaking model parameter degeneracies. Furthermore the mass dependence of the halo clustering is opposite to that of the number counts. On the one hand, less massive halos are less clustered than the massive ones; on the other hand, the former are more numerous. Thus a combined measurement allows for a better mass determination of the cluster sample and directly improves the parameter inference. This is a clear advantage of dedicated cluster surveys over serendipitous searches.
(6) Introducing a prior of 10% on the Hubble constant does not significantly improve w_a, w_0 for the final $dn/dz+\xi$ + Planck settings but some 40, 20% better constraints are predicted when only dn/dz + Planck are considered.
(7) We have examined the case where the M-L relation is perfectly known at all redshifts: we observe an improvement of less than 15% both on w_0 and w_a for the C20 population with the optimistic assumption.
(8) We have further investigated what happens if the dispersion in the M-L relation (which can be interpreted as the dispersion in any mass-observable relation) is decreased from 0.6 to 0.1, re-computing the priors accordingly. In this case, the improvement is $\sim$ 10%; assuming in addition that the M-L relation is perfectly known leads to a negligible improvement.
(9) We have assumed that the cluster luminosities evolve self-similarly, which tends to be supported by current observations (Maughan et al. 2008). Other scaling laws can be assumed like, for instance, no evolution, which implies that distant clusters are less luminous than in the self-similar hypothesis: this would decrease the number of detected high-z clusters. The impact of the cluster evolution hypothesis can be bracketed by the extreme case were no $z>1$ clusters are detected; in this case, the optimistic constraints on w_0, w_a would change from 0.40, 1.29 to 0.51, 1.67.
(10) Finally, assuming a flat w(z)CDM cosmology improves the determination of w_0 and w_a by about 5%. For a flat wCDM, we predict a precision of 0.040 for w with the C20 optimistic configuration (*Survey-A*) .

A general summary of the expected dark energy parameter uncertainties from future cluster surveys has been presented in the Dark Energy Task Force (DETF) document (Albrecht et al. 2006). This review study classifies the projected performances of cluster surveys into stage II, III and IV. Stage II corresponds to surveys

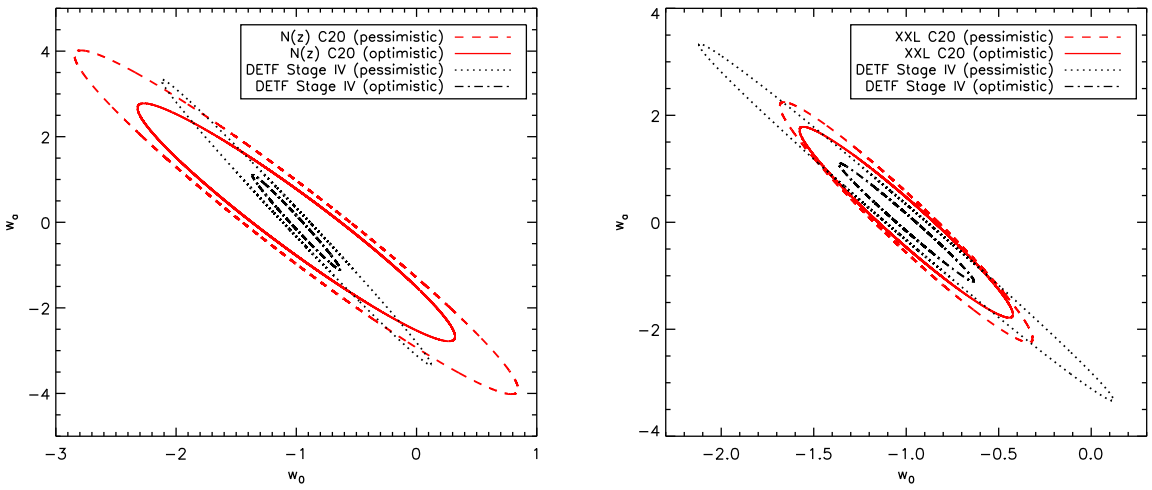


Figure 9. Illustration of the impact of the cluster-cluster correlation function - *A2 Survey* configuration (from Table 5). *Left*: 1-σ cosmological constraints from the cluster number counts only. *Right* Adding the correlation function. The black contours indicate the predictions by Dark Energy Task Force, stage IV .

of 200 $\deg^2$ with a mean mass threshold of $10^{14}h^{-1}\mathrm{M}_\odot$ detecting approximately $4000-5000$ clusters, and for which the expected errors on the dark energy parameters are $\sigma_{w_0}=1.1$ and $\sigma_{w_a}=3.2$. Stage III consists of surveys covering $4000\ \deg^2$ with a mean threshold of $10^{14.2}h^{-1}\mathrm{M}_\odot$ detecting $\sim 30,000$ clusters. Finally Stage IV corresponds to surveys covering $20,000\ \deg^2$ with a mass threshold of $10^{14.4}h^{-1}\mathrm{M}_\odot$ and providing also $30,000$ clusters.The DETF predictions for stage III and IV are recalled in Table 8; they are comparable for both stages as each of them appear to be dominated by systematics.

These projections have been derived under a number of assumptions which differ from ours. First, the halo mass function has been assumed in the fitting form provided by Jenkins et al. (2001). Second, the settings of the Fisher analysis are also slightly different: while both studies involve the same number of parameters, the analysis presented by Albrecht et al. (2006) assumes a prior of $\sim 10\%$ on the Hubble constant - we do not (they also consider the δ_ζ parameter ($k^3P_\zeta/2\pi^2$) in place of σ_8). Conversely, they use only number counts - we consider, in addition, the correlation function. The DETF adopts a constant mass selection, and masses are supposedly determined through "self-calibration", i.e. a functional dependence between flux (or richness), mass and redshift is assumed (see Majumdar & Mohr 2004). The DETF has further assumed a root mean square error in the mean/variance of mass per redshift bin ranging from $2-14\%$ for stage III and $1.6-11\%$ for stage IV. Despite these differences, it is worth comparing the performances advocated by the DETF with our predictions. A quick glance at Tables 5 and 8 immediately reveals that the XXL pessimistic predictions outperform the DETF pessimistic ones and that XXL optimistic ones lay between the optimistic and pessimistic DETF calculations. This is a somewhat unexpected result given the ratio of the surveyed areas (a factor of 80-400) but is readily understandable as the effect of the mass accuracy and of the presence of $z>1$ clusters, a direct consequence of the XMM deep exposures. We further compare the virtue of the XXL cluster population with the other cosmological probes examined by the DETF, namely : baryon acoustic oscillations, supernovae and weak lensing measurements. The comparisons are displayed in Fig. 10.

7 DISCUSSION AND CONCLUSIONS

We have shown through a Fisher matrix calculation that the XXL *Survey-A* (and *B*) can provide measurements of the cluster number counts and 2-point correlation function of sufficient precision to provide useful constraints on the equation of state of the dark energy. In our analysis, special care has been devoted to the realistic modeling of the statistical uncertainties (sample variance and shot noise) due to the small size of the surveyed area (50 or 200 $\deg^2$) and of the cluster mass measurements. Our experience gained with XMM has allowed us to consider realistic cluster selection functions and to apply priors on individual cluster mass measurements. We have favored this approach against the use of 'self-calibration' techniques, intended to by-pass the current ignorance about the evolution of the cluster scaling law by simultaneously fitting its functional form with cosmology. After all, self-calibration has not been observationally tested yet, and as shown by Sahlén et al. (2009), it is hampered by the fact that it introduces a latent degeneracy between the dispersion in the scaling laws and their redshift evolution. Moreover, it has been pointed out by Pacaud et al. (2007) that, in the case of X-ray flux measurements, emission lines produce discontinuities which cannot be simply accounted for by the parametrized functional dependence. On the basis of these considerations we have deliberately assumed to individually measure cluster masses, and improve the X-ray mass derivation by means of S-Z and weak lensing observations. This is a reasonable working assumption given the relatively limited size of the surveyed area and the results will form the ideal basis for investigating, a posteriori, self-calibration techniques. In the present analysis we have let the normalization of the scaling relation to be free for each $\Delta z=0.1$ redshift bins. Alternatively, taking larger bins (e.g. $\Delta z=0.2$) decreases the number of free parameters by a factor of two. This would allow the introduction of e.g. two more free parameters so as to enable the simultaneous fit of the evolution of the slope and of the dispersion of the relation. These hypotheses will be discussed in a subsequent article (paper II, Pacaud et al, in prep.). In this forthcoming work, we shall also compare the relative efficiency of various cluster selection functions (such as those presented here and a fixed mass limit at any redshift), investigate the role of plausible evolution laws other than self-similarity, examine

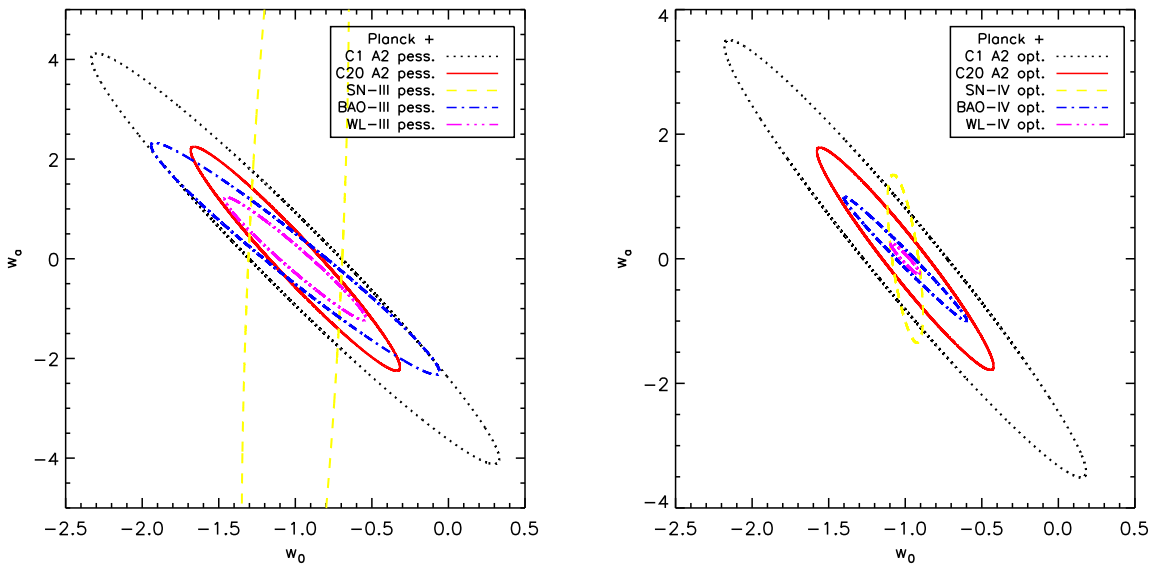


Figure 10. *Left*: the 1-σ contours in the w_0-w_a plane for the various DETF probes at stage III (pessimistic assumptions) along with the XXL predictions for the C1 and C20 populations (pessimistic case from Table 5). The contours for the DETF probes have been derived using the Fisher matrix data from the DETFast code, including the Planck priors in the same way as for XXL. *Right*, same as *Left* for the DETF stage IV and optimistic assumptions.

the impact of the DE inhomogeneities on the halo mass function, discuss the added value of the evolution of ξ and, especially, that of the cluster mass function ($dn/dMdz$) in constraining the DE equation of state.

In any case, our analysis demonstrates that a medium deep 50 deg^2 survey with XMM - a modest project compared to the DETF stage IV requirements - is in a position to fulfill competitive expectations in terms of cluster cosmological studies, while providing constraints which are complementary to those expected from other probes. Moreover, from a practical point of view, compared to the cluster surveys advocated by the DETF (Stage III and IV) the XXL survey contains some 20 times less clusters, which makes the sample much more tractable.

We have shown that the *Survey-A* and *Survey-B* configurations provide equivalent constraints on the DE for a similar amount of XMM observing time ($\sim$ 20 Ms). Practically, we favor configuration A over B as, besides constraining the properties of dark energy, it is observationally more advantageous. There are also a number of compelling arguments as to the "legacy value" of *Survey-A*, which make it more appealing. Let us review them in some detail.

- The aimed mass accuracy (to be complemented by a joint analysis of S-Z and weak lensing surveys), for all clusters entering the analysis, will have an invaluable scientific potential for the study of baryon physics. In particular, it will provide the long expected scaling law evolution out to a redshift of $\sim$ 1.5 and to a mass $M_{200} \sim 10^{14} M_{\odot}$. XMM pointed observations cannot achieve such an efficient determination for the simple reason that few X-ray clusters, and only massive ones, are known at $z \sim 1$. In contrast the *Survey-A* configuration has the ability to detect and reliably measure the signal from these objects in one single shot. This will provide very useful calibration data for other surveys (e.g. DES, eRosita), which are expected to cover much larger areas but at lower depth and poorer X-ray angular resolution (Predehl et al. 2006). Then the self-calibration method will be easily testable.

- The spatial distribution of X-ray AGNs, which will constitute more than 90% of the sources of the planed survey, will be studied on very large scales as a function of their spectral properties.

- For visibility reasons and observation programming, we favor the splitting of *Survey-A* in two or four sub-regions spread in right ascension. Furthermore, the XMM observations can be scheduled over four years, with each field being entirely covered by 10 ks XMM observations every year. The first year scan could already provide the full C1 + C2 cluster catalogue, hence measurements of ξ and dn/dz and constraints on the DE to an accuracy half of the final value. The three subsequent scans will then increase the number of X-ray photons down to the nominal 40 ks depth, thus providing the spectral accuracy and, finally, the cluster mass accuracy required for the full cosmological analysis.

- Spreading the XMM observations over four years can provide unrivaled information about AGN variability over large timescales as a function of the spectral properties and environment.

Finally, in addition to the important added value of ξ, we mention a number of arguments leading to favor contiguous surveys with respect to serendipitous cluster searches:

- Operationally it is much more efficient to perform a joint X-ray + optical/lensing + S-Z survey than to undertake a pointed follow-up of X-ray clusters. And obviously, a joint optical survey renders the X-ray source identification straightforward.

- Homogeneous wide surveys, compared to serendipitous searches, highly simplify the derivation of the selection functions which, as shown here, play a critical role for cosmological studies.

- Using XMM archival data would only allow the determination of dn/dz and it is moreover important to note that the situation is different from that of the ROSAT serendipitous searches. ROSAT had a two-degree diameter field of view (against 30 arcmin for XMM) and a significant fraction of the known cluster population has been imaged by XMM[7]. This introduces complex biases that

[7] Over 1 000 cluster observations performed. Out of the some 1600 obser-

cannot be removed by simply discarding the central target or ignoring the target clusters as was routinely assumed in the past; it is especially serious at high redshift since only the X-ray brightest known clusters were considered as targets.
- The proposed homogeneous survey will also enable the determination of the structure of the X-ray background on very large scales at energies ranging from 0.1 to 10 keV. In addition, once the cluster population is detected and the redshifts measured, their 3-D distribution will enable the identification of putative cosmic filaments. Staking the X-ray data corresponding to the location of many filaments then could lead to the first detection of the Warm Hot Intergalactic Medium in emission (Soltan 2008).

One of the interesting outcomes of the present study is to have quantitatively estimated the impact of the cluster-cluster correlation function in dark energy studies. We leave to future studies the possibility of measuring the evolution of the cluster mass function $dn/dMdz$ rather than dn/dz with the XXL survey, as well as the combination with the low-z REFLEX correlation function and the Planck cluster number counts + correlation function. In the future, one can also well imagine constraining cosmology directly by applying the X-ray selection function on a large set of hydrodynamical simulations - when these become achievable - and match the properties of the resulting simulated cluster catalogues to that of the observed XXL one. Such methods, which are already applied on the Lyα forest (Viel & Haehnelt 2006) would allow one to totally by-pass the determination of the cluster mass-observable relations as a function of redshift.

ACKNOWLEDGMENTS

We acknowledge numerous discussions which took place during the XXL meeting, held in Paris in April 2008 and from which the XXL survey concept emerged. We would like to thank the authors of Pinocchio, especially P. L. Monaco, for their help and support on their software. We thank Romain Teyssier for having provided us with the Horizon cluster catalogue. We are grateful to Anaïs Rassat and Alexandre Refregier for many useful technical discussions and to Jim Rich for helpful comments on the manuscript. Part of this work is financed by a grant from the Centre National d'Etudes Spatiales. FP acknowledges support from the Transregio Programme TR33 of the Deutsche Forschungsgemeinschaft and from the grant 50 OR 1003 of the Deutsches Zentrum für Luft- und Raumfahrt.

vations available with exposure time longer than 40ks (any type of targets), about 400 useful images remain when considering only high galactic latitude public observations and assuming a flaring rate of 25% (status of the XMM archive by September 2010)

Table 5. Cosmological constraints. Survey configuration A2 - 50 deg^2 full depth (40 ks XMM exposures) 1-σ errors on w_0 / w_a

		Pessimistic mass measurements		Optimistic mass measurements	
Selection	Redshift range	dn/dz + Planck	dn/dz + ξ + Planck	dn/dz + Planck	dn/dz + ξ + Planck
C1	$0 < z < 1$	2.38 / 5.08	0.88 / 2.71	1.98 / 4.15	0.78 / 2.32
C2	$0 < z < 1$	2.00 / 4.64	0.72 / 2.36	1.70 / 3. 89	0.65 / 2.06
C20	$0 < z < 2$	1.19 / 2.59	0.45 / 1.46	0.87 / 1.82	**0.38 / 1.18**

Table 6. Cosmological constraints. Survey configuration B0 - 200 deg^2 full depth (10 ks XMM exposures) 1-σ errors on w_0 / w_a

		Pessimistic mass measurements		Optimistic mass measurements	
Selection	Redshift range	dn/dz + Planck	dn/dz + ξ + Planck	dn/dz + Planck	dn/dz + ξ + Planck
C1	$0 < z < 1$	1.58 / 3.30	0.54 / 1.71	1.33 / 2.72	0.48 / 1.47
C2	$0 < z < 1$	1.42 / 3.29	0.47 / 1.60	1.13 / 2.52	**0.40 / 1.29**

Table 7. Cosmological constraints. Survey configuration A2 - 50 deg^2 1/4 depth (10 ks XMM exposures) 1-σ errors on w_0 / w_a

Selection	Redshift range	dn/dz + Planck	dn/dz + ξ + Planck
C1 (pessimistic)	$0 < z < 1$	2.77 / 5.98	**0.97 / 3.08**
C2 (optimistic)	$0 < z < 2$	1.14 / 2.44	**0.55 / 1.70**

Table 8. Cosmological constraints from clusters following the DETF survey designs 1-σ errors on w_0 / w_a

Stage	Pessimistic	Optimistic
III	0.70 / 2.11	0.26 / 0.77
IV	0.73 / 2.18	0.24 / 0.73

REFERENCES

Alimi, J.-M., Fuzfa, A., Rasera, Y., Courtin, J. & Corasaniti, P.-S. arXiv:0903.5490

Abramo, L. R., Batista, R. C., Liberato, L., & Rosenfeld, R. 2007, JCAP, 0711, 012

Albrecht, A., et al. 2006, arXiv:astro-ph/0609591

Allen, S. W., Schmidt, R. W., Fabian, A. C., Ebeling, H., 2003, MNRAS 342, 287

Allen, S. W., Rapetti, D. A., Schmidt, R. W., et al., 2008, MNRAS 383, 879

Arnaud, M., & Evrard, A. E. 1999, MNRAS, 305, 631

Arnaud, M., Pointecouteau, E., & Pratt, G. W. 2005, A&A, 441, 893

Bahcall, N. A., et al. 2003, ApJ, 585, 182

Baldi, M., & Pettorino, V. 2010, arXiv:1006.3761

Basilakos, S., Plionis, M., & Lima, J. A. S. 2010, arXiv:1006.3418

Bean, R. & Doré, O. 2004, PRD, 69, 083503

Bond, J. R., Cole, S., Efstathiou, G., & Kaiser, N. 1991, ApJ, 379, 440

Borgani, S., et al. 2001, ApJ, 561, 13

Courtin, J., Rasera, Y., Alimi, J. -., Corasaniti, P. -., Boucher, V., & Fuzfa, A. 2010, arXiv:1001.3425

Cunha, C. E., & Evrard, A. E. 2009, arXiv:0908.0526

Chevallier, M. & Polarski, D. 2001, Int.J. Mod. Phys. D, 10, 213

De Bernardis, P. 2000, Nature, 404, 955

Dunkley, J., et al. 2009, ApJS, 180, 306

Eisenstein, D. J., & Hu, W. 1998, ApJ, 496, 605

Eisenstein, D. J., Hu, W., & Tegmark, M. 1999, ApJ, 518, 2

Eke, V. R., Cole, S., Frenk, C. S., & Henry, J. P. 1998, MNRAS, 298, 1145

Evrard, A. E. 1989, ApJ, 341, L71

Gioia, I. M., Henry, J. P., Maccacaro, T., Morris, S. L., Stocke, J. T., & Wolter, A. 1990, ApJ, 356, L35

Finoguenov, A., et al. 2007, ApJS, 172, 182

Giacconi R., et al., 2009, arXiv:0902.4857 879

Gladders, M. D., et al. 2007, ApJ, 655, 128

Haiman, Z., Mohr, J. J., & Holder, G. P. 2001, ApJ, 553, 545

Henry, J. P. 1997, ApJ, 489, L1

Henry, J. P. 2000, ApJ, 534, 565

Henry, J. P. 2004, ApJ, 609, 603

Henry, J. P., Evrard, A. E., Hoekstra, H., et al., 2009, ApJ691, 1307

Holder, G.P. Mohr, J.J., Carlstrom, J.E, Evrard, A.E. and Leitch, E.M. 2000, ApJ, 544, 629

Holder, Z. Haiman & G.P. Mohr 2001, ApJ, 560, L111

Hu, W. & Kravtsov, A. V. 2003, ApJ, 584 702

Hu, W., & Cohn, J. D. 2006, Phys. Rev. D, 73, 067301

Hütsi, G. 2010, MNRAS, 401, 2477

Huterer, D. & Turner, M. 2001, PRD, 64, 123527

Jenkins, A. et al. 2001, MNRAS, 321, 372

Koester, B. P., et al. 2007, ApJ, 660, 239

Kosowsky, A., Milosavljevic, M., & Jimenez, R. 2002, Phys. Rev. D, 66, 063007

Kravtsov, A. V., Vikhlinin, A., & Nagai, D. 2006, ApJ, 650, 128

Landy, S. D., Szalay, A. S., 1993, ApJ412, 64

Larson, D., et al. 2010, arXiv:1001.4635

Lima, M., & Hu, W. 2005, Phys. Rev. D, 72, 043006

Linder, E. V. 2003, PRL, 90, 91301

Lin, Y.-T. & Mohr, J.J. 2003, ApJ, 582, 574

Mahdavi, A., Hoekstra, H., Babul, A., et al., 2007, ApJ664, 162

Majumdar, S. & Mohr, J. J. 2003, ApJ, 585, 603

Majumdar, S. & Mohr, J. J. 2004, ApJ, 613, 41

Mantz, A., Allen, S. W., Ebeling, H., & Rapetti, D. 2008, MNRAS, 387, 1179

Matarrese, S., Coles, P., Lucchin, F., & Moscardini, L. 1997, MNRAS, 286, 115

Mo, H. J. & White, S. D. M. 1996, MNRAS, 282, 347

Monaco, P., Theuns, T., & Taffoni, G. 2002a, MNRAS, 331, 587

Monaco, P., Theuns, T., Taffoni, G., Governato, F., Quinn, T., & Stadel, J. 2002b, ApJ, 564, 8

Mota, D. F. & Van der Bruck, C. 2004, A&A, 421, 71

Mukherjee, P., Parkinson, D., Corasaniti, P.S., Liddle, A.R. & Kunz, M. 2006, MNRAS, 369, 1725

Navarro, J. F., Frenk, C. S., & White, S. D. M. 1997, ApJ, 490, 493

Maughan, B. J., et al. 2008, MNRAS, 387, 998

Mazure, A., et al. 2007, A&A, 467, 49

Oukbir, J. & Blanchard, A. 1992, A&A, 262, L21

Pacaud, F., Pierre, M., Refregier, A., et al., 2006, MNRAS372, 578

Pacaud, F., Pierre, M., Adami, C., et al., 2007, MNRAS382, 1289

Percival, W.J., et al. 2001, MNRAS, 327, 1297

Pierre, M., et al. 2004, Journal of Cosmology and Astro-Particle Physics, 9, 11

Pierre, M., Pacaud, F., Duc, P.-A., et al., 2006, MNRAS372, 591

Predehl, P., et al. 2006, Proc. SPIE, 6266, 19

Press, W. H. & Schechter, P. 1974, ApJ, 187, 425

Rozo, E., et al. 2007, astro-ph/0703571

Rozo, E., et al. 2009, arXiv:0902.3702

Sahlén, M., et al. 2009, MNRAS, 397, 577

Schuecker, P., Böhringer, H., Collins, C. A., Guzzo, L., 2003, A&A398, 867

Scharf, C. 2002, ApJ, 572, 157

Seljak, U. & Zaldarriaga, M. 1996, ApJ, 469, 437

Sheth, R. K. & Tormen, G. 1999, MNRAS, 308, 119

Soltan, A. M. 2008, Pathways Through an Eclectic Universe, 390, 364

Spergel, D.N. et al. 2003, ApJS, 148, 175

Stanek, R., Evrard, A. E., Böhringer, H., et al., 2006, ApJ648, 956

Taffoni, G., Monaco, P., & Theuns, T. 2002, MNRAS, 333, 623

Tegmark, M., Taylor, A., & Heavens, A. 1997, ApJ, 480, 22

Tegmark, M., et al. 2004, ApJ, 606, 702

Teyssier, R., et al. 2009, A&A, 497, 335

Tinker, J. et al. 2008, ApJ, 688, 709

Tinker, J. L., Robertson, B. E., Kravtsov, A. V., Klypin, A., Warren, M. S., Yepes, G., & Gottlober, S. 2010, arXiv:1001.3162v2

Viana, P. T. P. & Liddle, A. R. 1996, MNRAS, 281, 323

Viel, M., & Haehnelt, M. G. 2006, MNRAS, 365, 231

Vikhlinin, A., et al. 2003, ApJ, 590, 15

Vikhlinin, A., et al. 2009, ApJ, 692, 1060

Wang, L. & Steinhardt, P. J. 1998, ApJ, 508, 483

Wang, S. et al. 2004, PRD, 70, 123008

Weller, J., Battye, R., & Kneissl, R. 2002, PRL, 88, 231301

White, S. D. M., Efstathiou, G., & Frenk, C. S. 1993, MNRAS, 262, 1023

Yu, H.-Y., Rozo, E., & Wechsler, R. H. 2008, ApJ, 688, 729

Wu, H.-Y., Rozo, E., & Wechsler, R. H. 2010, ApJ, 713, 1207

Zaldarriaga, M. & Seljak, U. 1997, PRD, 55, 1830

APPENDIX A: ADOPTED HALO MASS FUNCTION

Early modeling of the mass function relied on semi-analytical approaches (Press & Schechter 1974; Bond et al. 1991), however comparison with N-body simulations showed discrepancies with the numerically estimated function, and a simulation calibrated formula was proposed by Sheth & Tormen (1999). Over the years the increasing resolution of numerical simulations has led to more accurate estimations of the halo mass function, and the standard of accuracy has been set by the analysis of Jenkins et al. (2001). The authors of this study have provided a 'universal' (hence applicable to different cosmologies and at different redshifts) fitting formula that is accurate to within 20%. Recent studies have cast doubts on the universality of the mass function. In particular the analysis by Tinker et al. (2008) has shown important deviations in the high mass end and at high redshift. Nonetheless these authors have been able to provide a fitting formula accurate to $< 5\%$ at $z = 0$ and to $< 20\%$ at $z = 1.25$, while degrading to 50% only at $z = 2.5$. In our analysis we assume their fitting halo mass function, parametrized in terms of the halo mass enclosed in a radius containing 200 times the critical density of matter, $\mathbf{M_{200c}}$, with the following functional form,

$$f(\sigma, z) = A \left[\left(\frac{\sigma}{b} \right)^{-a} + 1 \right] e^{-c/\sigma^2}, \qquad \text{(A1)}$$

where $A = A_0(1+z)^{-0.14}$, $a = a_0(1+z)^{-0.06}$, $b = b_0(1+z)^{-\alpha}$ and $\log_{10}\alpha = -\left[0.75/\log_{10}\left(2.67/\Omega_{\rm m}(z)\right)\right]^{1.2}$, (see Eqs. (3)-(8) in Tinker et al. 2008). In Table 2 of the same paper, values of the parameters A_0, a_0, b_0 and c are provided for several density contrasts $\Delta_{\rm m}$, defined with respect to the mean matter density. Following the guidelines of their Appendix B, we perform spline interpolation between the individual parameter values to match our mass overdensity convention $\Delta_{\rm m} = 200/\Omega_{\rm m}(z)$ at any given z. This ensures that the mass definition of our cosmological modeling matches the convention used for cluster scaling relations and thus for our selection function.

It has recently been pointed out that DE leaves characteristic imprints on the non-linear phase of collapse of halos. These imprints manifest in the non-linear power spectrum as well as in the halo mass function and may yield up to 20% deviations from ΛCDM predictions (Courtin et al. 2010). In paper II (Pacaud et al, in prep.) we shall investigate how this would impact the predicted DE constraints.

APPENDIX B: EVALUATING THE SIGNIFICANCE OF dn/dz AND ξ FOR VARIOUS SURVEY CONFIGURATIONS

We use the publicly available Pinocchio package (Monaco et al. 2002a,b; Taffoni et al. 2002) to generate 3D cluster catalogues for a given initial density field realisation and cosmology. We use the 2.2-beta version, that is now entirely paralleled and available from the authors on demand. Pinocchio, while following the procedure of N-body simulations, works in the Zel'dovich approximation, allowing for faster computation by several orders of magnitude with respect to equivalent N-body simulations (in terms of mass resolution and volume probed). Confronting the Pinocchio realisations with the high resolution full-sky Horizon simulations (Teyssier et al. 2009) (in the case of a ΛCDM model best-fit to WMAP-3 years data) we have checked that the Pinocchio cluster mass function is accurate to 10%, and that the 2-point correlation function can be reliably estimated down to $10h^{-1}\mathrm{Mpc}$ scale. We observe however, a slight increase of ξ around this scale, as the unresolved clusters tend to accumulate at this point. We illustrate below our procedure considering the C2 selection for various configurations totalling the 50 deg^2 of *Survey-A*.

Table B1. Surveys extracted from the *Pinocchio* simulations. Fields A0, A1, A2 pertains to different configurations of *Survey-A* totalling 50 deg^2. Field Z1 covers 10 000 deg^2 and is used for statistical comparison.

survey configurations	A0	A1	A2	Z1
Total surveyed area (deg^2)	50	50	50	10 000
number of sub-fields	1	2	4	4
sub-field side (in deg)	7.07	5	3.54	50
number of independent simulated sub-fields	190	215	230	30

Using Pinocchio we generate 5 cosmic volumes with different random initial conditions for a ΛCDM model best-fitting WMAP-5 years data (Dunkley et al. 2009). Each volume is a box of $3500 \times 3500 \times 3500$ comobile Mpc^3 observed from the corners, providing 8 past-lightcone octants. These octants are combined, using the periodicity of the volumes, to finally provide 5 full-sky past-lightcones independant from each other. The physical position of each simulated halo is corrected for its peculiar velocity since the correlation function is computed in redshift space. In order to estimate the halo 2-point correlation function 5 bootstrap full-sky lightcones are generated from the data. The angular position of each halo is randomized 10 times to artificially create lightcones containing 10 times more halos than the original data. The redshifts of the original Pinocchio simulated data as well as the mass probability distribution function are conserved in these "random" lightcones.

From these lightcones we extract a large number of XXL survey realisations. We considered several survey configurations: a single 7.07×7.07 deg^2 field, and configurations consisting of two 5×5 deg^2 and four 3.54×3.54 deg^2 patches respectively. The last two configurations are more likely to correspond to actual observations since spreading patches in right ascension ensures a more efficient observation scheduling. Also splitting the survey into several sub-fields is usually expected to decrease the impact of the sample variance; an effect that we quantitatively estimate hereafter. In order to avoid large-scale correlations, edges of the extracted sub-fields are separated by at least 30 deg in RA and Dec. We also extracted survey fields covering 50x50 deg^2 for statistical comparison. The characteristics of the different survey realisations are given in Table B1.

In each simulated sub-field, we compute dn/dz and ξ, for a given selection. The 2-point correlation fuction is measured using the estimator introduced by Landy & Szalay (1993). The results are then combined according to each of the survey configurations illustrated in Table B1; e.g. for the A2 design, individual dn/dz are summed over the 4 patches, while individual ξ are averaged over the ensemble. Then for each configuration, the resulting quantities are averaged over all realisations. The 1σ errors about the average dn/dz and ξ are computed as a function of z and R for each of the 4 survey configurations, including the signal-to-noise ratio. As we describe in Section 5 we use the estimated values of S/N to determine the experimental uncertainties necessary for the Fisher matrix analysis. Results are summarized in Figs. B1 and B2. As it can be appreciated from Fig. B1, the cluster number counts turn out to be

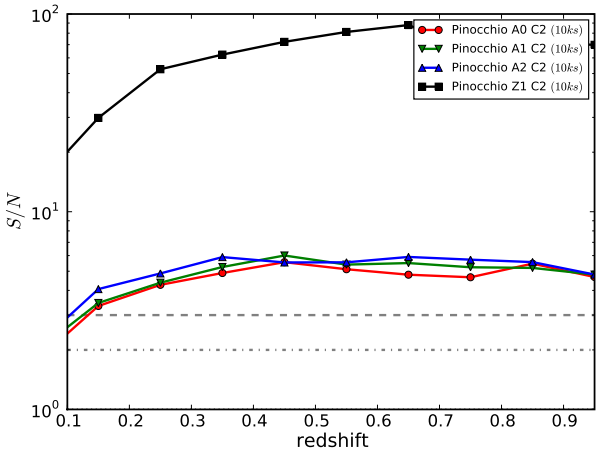


Figure B1. Signal-to-noise ratio for dn/dz as a function of redshift, obtained for different realisations of *Survey-A* and the C2 selection using Pinocchio simulations; bin size $\Delta z = 0.1$

insensitive to the sub-field splitting of the survey design, i.e. a single 7.07×7.07 deg^2 field (A1), two 5×5 deg^2 sub-fields (A1) or four 3.54×3.54 deg^2 sub-fields (A2). The 2-point correlation function appears to be slightly dependent on the size of the sub-fields but the impact on the S/N is negligible. The 50×50 deg^2 Z1 reference realization indicates that it is possible to reliably compute ξ at least out to 40 Mpc/h for the A0, A1 or A2 configurations. We note that 40 h^{-1}Mpc is slightly smaller than the comoving length encompassed by the A2 realisation at the survey maximum sensitivity (3.54 deg at $z = 0.3$ corresponds to 53 h^{-1}Mpc scale). We sample ξ with a scale separation $> 10h^{-1}$Mpc because of the limited resolution of the Pinocchio simulations. Since cluster virial radii are on the order of $1h^{-1}$ Mpc, this implies that we may be loosing some power on scales of $\sim 5 - 10h^{-1}$ Mpc, where mergers are expected to occur.

The Pinocchio experiment indicates the A0, A1 and A2 configurations are equivalent in terms of S/N both for dn/dz and ξ. In the paper we consider the A2 configuration, which is for observational reason the easiest to perform, when presenting the results of the cosmological analysis.

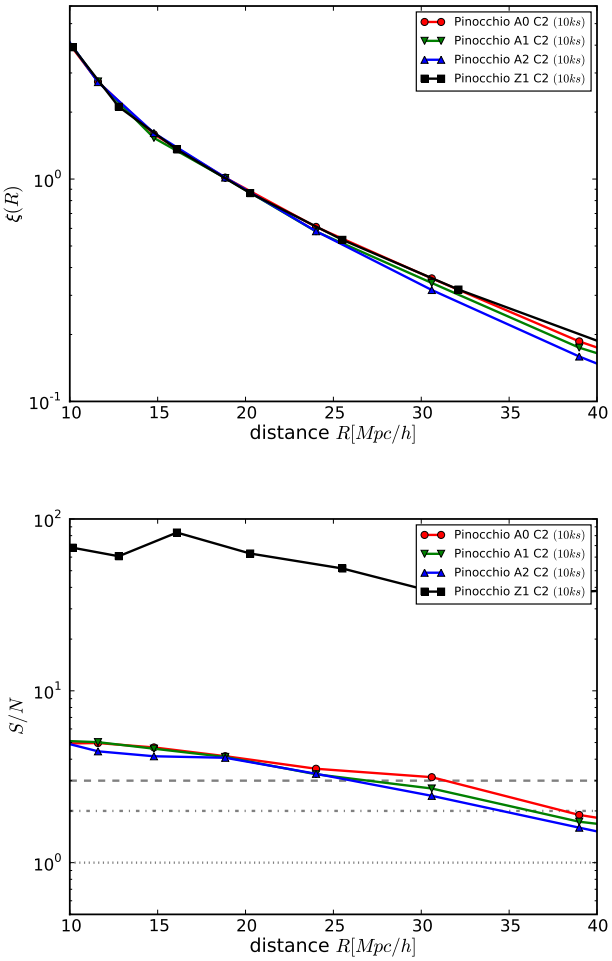


Figure B2. *Top*: 3D averaged 2-point correlation function for different *Survey-A* realisations extracted from the Pinocchio simulations using the C2 selection function. The bin size is $d \log R = 0.1$. *Bottom*: Corresponding signal-to-noise ratio.